Energy 262 (2023) 125531

Contents lists available at ScienceDirect

Energy

journal homepage: www.elsevier.com/locate/energy

Efficient X-ray CT-based numerical computations of structural and mass transport properties of nickel foam-based GDLs for PEFCs

Mustafa Ercelik [a], Mohammed S. Ismail [a,b,*], Derek B. Ingham [a], Kevin J. Hughes [a,**], Lin Ma [a], Mohamed Pourkashanian [a,b]

[a] Energy 2050, Department of Mechanical Engineering, Faculty of Engineering, The University of Sheffield, Sheffield, S3 7RD, United Kingdom
[b] Translational Energy Research Centre (TERC), University of Sheffield, Sheffield, S9 1ZA, United Kingdom

ARTICLE INFO

Keywords:
Polymer electrolyte fuel cell
Gas diffusion layer
Nickel foam
X-ray computed tomography
Structural characteristics
Mass transport characteristics

ABSTRACT

Nickel foams are excellent candidate materials for gas diffusion layers (GDLs) for polymer electrolyte fuel cells (PEFCs) and this is due to their superior structural and transport properties. A highly computationally-efficient framework has been developed to not only estimate the key structural and mass transport properties but also to examine the multi-dimensional uniformity and/or the isotropy of these properties. Specifically, multiple two-dimensional X-ray CT images and/or numerical models have been used to computationally determine the porosity, the tortuosity, the pore size distribution, the ligament thickness, the specific surface area, the gas permeability and the effective diffusivity of a typical nickel foam sample. The results show that, compared to the conventionally used carbon substrate, the nickel foam sample demonstrate a high degree of uniformity and isotropy and that it has superior structural and mass transport properties, thus underpinning its candidacy as a GDL material for PEFCs. All the computationally-estimated properties, which were found to be consistent with the corresponding literature data, have been presented and thoroughly discussed.

1. Introduction

The polymer electrolyte fuel cell (PEFC), which directly converts the chemical energy of hydrogen and oxygen into electrical energy, is a favourable power source for a multitude of portable, stationary and automotive applications [1–6]. A wet-proofing, porous layer located between the catalyst layer and flow-field plate is termed as the gas diffusion layer (GDL) [7,8]. The main functions of the gas diffusion layers are to: (i) supply reactant gases of oxygen and hydrogen to the active areas in the catalyst layer, (ii) mitigate the detrimental impact of excess water and (iii) electrically connect between the catalyst layers and the flow field plates to power the external load [9–11].

Water (mostly in the form of liquid) is produced as a by-product of the oxygen reduction reaction (ORR) taking place at the cathode catalyst layer. Furthermore, the reactant gasses fed to the fuel cell are mostly humidified to ensure the initial humidification of the membrane electrolyte. Insufficient or excess amount of water are both detrimental for the operation of the fuel cell. Namely, an insufficient amount of water causes the membrane to dry out, and subsequently reduce the membrane ionic conductivity. On the other hand, an excess amount of water, which is likely to occur at high current densities, induces flooding which may partially/completely block the voids within the GDL and hinder the transport of the reactant gases to the catalyst layers, thus resulting in mass transport losses [12–16]. These losses are more detrimental while the PEFC is operated at the saturated conditions. To this end, water management in PEFC (particularly at its cathode) is highly crucial for its sustainable operation.

The commercially available GDLs are customarily made of electrically conductive carbon fibre-based materials and they are often made in the form of carbon papers or carbon cloths [17–19]. However, such materials are likely to be, due to their low mechanical strength, subject to different types of degradation: mechanical degradation due to compression; thermal degradation arising from freeze/thaw cycles; dissolution; and erosion caused by the flow of gases [20–22]. Hence, many studies have been conducted to explore and investigate alternative materials for the GDLs.

* Corresponding author. Energy 2050, Department of Mechanical Engineering, Faculty of Engineering, The University of Sheffield, Sheffield, S3 7RD, United Kingdom.
** Corresponding author.
E-mail addresses: m.s.ismail@sheffield.ac.uk, msaeedaaal@gmail.com (M.S. Ismail), k.j.hughes@sheffield.ac.uk (K.J. Hughes).

https://doi.org/10.1016/j.energy.2022.125531
Received 1 April 2022; Received in revised form 1 August 2022; Accepted 20 September 2022
Available online 23 September 2022

Metal foam-based materials have attracted a great deal of attention as promising components in a variety of energy and engineering related applications such as: filtration and separation, heat exchangers, flow distributors, thermal energy storage, heat pipes, electrolysers, catalyst supports, lithium-ion batteries, etc. [23–32]. Recent studies have reported that nickel foams are promising materials that could be used as PEFC cathode flow field plates (FFPs) and/or GDLs and this is, compared to the conventionally-used materials, due to their higher: volume-to-weight ratio, cost effectiveness, electrical and thermal conductivity, porosity and specific surface area [33–36]. Some recent investigations experimentally explored the potential use of the nickel foam as a cathode FFP and showed that such a FFP demonstrates better fuel cell performance and durability than those of the conventional graphite FFPs [35,37–42]. For instance, Shin et al. [41] experimentally tested a PEFC equipped with various nickel foam-based cathode FFPs and compared it with that running with a conventional graphitic serpentine FFP. They showed that the fuel cells operating with nickel foam cathode FFP are more stable and demonstrates a 50.6% better performance than that of the graphitic serpentine FFP. Likewise, similar findings were reported by Liu et al. [42] who indicated that the catalytic activity and gas diffusion are likely to increase when using cathode nickel foam FFPs.

The PEFC performance is highly influenced by the structural and effective transport characteristics of the GDLs and as such it is important to estimate these characteristics and subsequently understand how various quantities are transported within the GDLs [43]. A variety of methods are used to estimate the structural GDL characteristics and the following are some examples [3]. Mercury intrusion porosimetry (MIP) is widely used to determine the GDL porosity and the pore size distribution; see for example [44–46]. Under vacuum conditions, gradually-increased pressure is applied to force the non-wetting mercury to penetrate the pores and subsequently determine the pore size distribution and the porosity of the porous media. The superficial two-dimensional images generated by the scanning electron microscopy (SEM) are often used to measure the thickness of the fibres; see for example [47]. However, these superficial images do not necessarily provide accurate measurement of the fibre thickness. The Brunauer–Emmett–Teller (BET) absorption method is normally used to estimate the specific area of the GDL materials, e.g. Refs. [48,49]. Most of the characterisation techniques, including the above mentioned ones, provide some "global" properties of the investigated material [50]; however, they do not resolve the heterogeneity of some materials that often lead to significant anisotropic transport properties as is the case for typical GDL materials.

X-ray computed tomography (CT) has been a handy tool to resolve the nano- or micro-scale local structural variation within the investigated PEFC materials, including the GDLs. Compared to other similar techniques, the X-ray CT technique is (i) non-destructive, (ii) quick and accurate, (iii) cost-effective and (iv) enable the examination under the realistic working conditions [51–53]. The micro-structure of the carbon fibre based GDL has been extensively investigated using X-ray CT. For example, Zenyuk et al. [54], Fishman et al. [45,55,56], James et al. [57], Meyer et al. [58,59], Fazeli et al. [60], and Garcia-Salaberri et al. [61] used X-ray CT to determine the structure-related properties such as porosity, tortuosity and pore size distribution. On the other hand, the microstructure of nickel foams as alternative materials for PEFCs was investigated using X-ray CT in several studies [62–65]. For instance, Fly et al. [63] performed imaging using the μ-X-ray CT and conducted electrochemical and mechanical tests to investigate the potential use of nickel foam as a FFP. The X-ray CT images show that the contact area between the nickel foam and the carbon paper GDL is ten times higher than that between the nickel foam and the stainless-steel FFP. Furthermore, the X-ray CT-based 3D models have also been employed to determine the structural and transport characteristics of the carbon-based and metal foam-based materials [66–68]. However, these 3D models require high computational resources and are very computationally expensive. To reduce the computational time, some researchers [69,70] have investigated the structural properties of some conventional GDL materials using a two-dimensional Lattice-Boltzmann model that was created by employing SEM images. However, the SEM images do not provide information regarding the interior structure of the investigated material.

To the best of the authors' knowledge, there have been no in depth studies on the structural and the transport characteristics of the nickel foams as potentially-used GDLs in PEFCs. Therefore, the characteristics of a typical nickel foam have been estimated using a workflow that involves imaging using an X-ray CT facility, image processing and numerical modelling. In this paper, the non-uniformity of the material has been innovatively resolved through solving multiple computationally-economic two-dimensional models representing some local slices of nickel foam within the imaged structure. The estimated properties using the above workflow (i.e. imaging, image processing and numerical modelling) have been presented and discussed.

2. Methodology

2.1. X-ray CT and image processing

X-ray CT images were captured using the SKYSCAN 1172 X-ray microscopy platform (Bruker, US). The platform comprises: an X-ray source, a rotational stage with a specimen holder and an X-ray detector to measure the X-ray density (Fig. 1). A commercially-available nickel foam sheet with 99.5% purity (GoodFellow Cambridge Ltd., the UK) was punched, creating 12.7 mm-diameter samples. The specimen was fixed on the rotational stage in the through-plane direction by a plastic-made apparatus. The emitted X-ray from the source crosses throughout the sample and then the detector that is located next to the rotational stage collects it. The scan was performed every time that the stage was rotated by 0.7° until the full 180° rotation was reached. The exposure time was 0.885 s and 1025 projections (i.e. two-dimensional slices) were collected. The source voltage was 80 kV and the beam current was 124 μA. The image resolution was 7 μm per pixel.

The captured slices were 2D grey shadows and were processed by the NRecon Reconstruction (SKYSCAN, Belgium) software to reconstruct the cross-section images from the X-ray CT projection images and Bruker CTan Micro-CT software to threshold the slices. To discriminate between the gaseous and solid phases, Otsu's thresholding method was used. The processed images were imported to COMSOL Multiphysics® 5.5 using MATLAB® and LiveLink™ for MATLAB®.

2.2. Numerical modelling

The continuity equation and conservation of momentum equation were, using COMSOL Multiphysics® 5.5, solved for 20 two-dimensional computational domains representing 20 equally-spaced scanned slices taken within 350 μm distance of the scanned nickel foam sample. The length and height of each slice are 6.65 and 1.05 mm, respectively. The flow within the computational domains was assumed to be steady-state, laminar (Reynolds numbers $\ll$ 2300) and incompressible (Mach numbers $\ll$ 0.3) and as such the continuity and momentum equations are expressed as follows:

$$\nabla \bullet (\rho \boldsymbol{u}) = 0 \tag{1}$$

where ∇ is the operator $(\frac{\partial}{\partial x} + \frac{\partial}{\partial y})$, ρ is the fluid density (kg/m^3), and $\boldsymbol{u}$ is the velocity vector.

$$\rho(\boldsymbol{u} \bullet \nabla)\boldsymbol{u} = \nabla \bullet \left[-p\boldsymbol{I} + \mu\left(\nabla \boldsymbol{u} + (\nabla \boldsymbol{u})^T\right) - \frac{2}{3}\mu(\nabla \bullet \boldsymbol{u})\boldsymbol{I} \right] \tag{2}$$

where p is the pressure, $\boldsymbol{I}$ is the identity matrix, and μ is the dynamic viscosity (Pa·s). The conservation of chemical species (oxygen gas in our case) is given by:

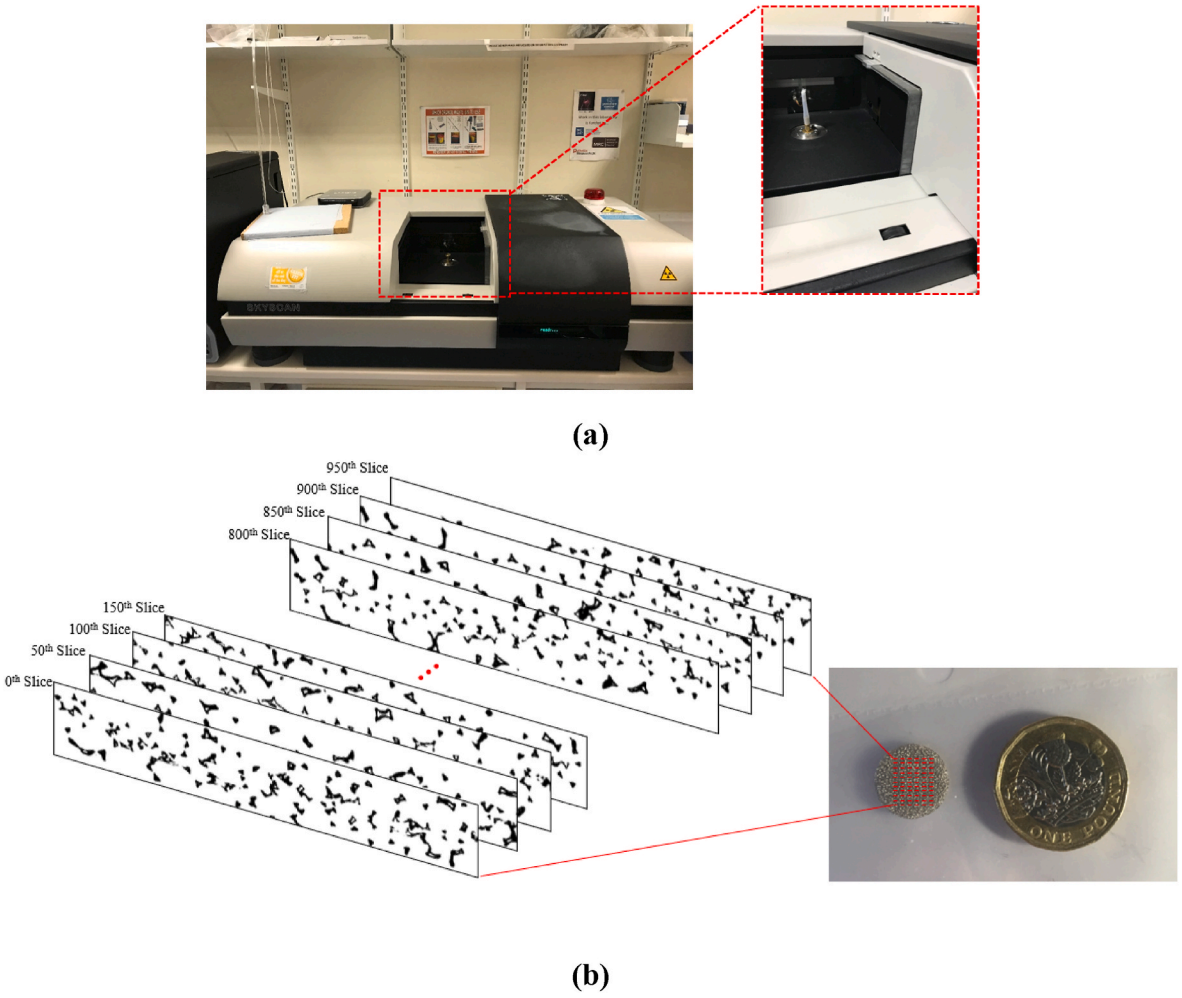

Fig. 1. Photographs of (a) the SKYSCAN X-ray CT platform and (b) the obtained two-dimensional slices.

$$\nabla \bullet (-D_{O2}\nabla C_{O2}) = R \tag{3}$$

where D_{O2} is oxygen diffusion coefficient (cm^2/s), C_{O2} is the oxygen concentration (mol/m^3), and R is the source term which is zero in our case (there is no reaction taking place within the GDL).

The 2D meshing procedure is conducted for each of the 20 slices using the COMSOL Multiphysics® 5.5 software. To ensure mesh-independent solutions, the number of elements has been systemically changed and the property of interest has been computed for all the various meshes and the computation time has been observed for the all the corresponding meshes. For example, Fig. 2 shows how the computed through- and in-plane gas permeability and the corresponding computation time changes with the number for elements for the 200th CT slice. The figure shows that the computed permeability values become almost insensitive to the number of elements with around 600,000 elements (the corresponding times are reasonably short: 100–200 s). The mesh independency test has been performed for all the 20 equally-spaced CT nickel foam slices and the minimum number of elements that achieves the mesh-independent solution was found to be between 400,000 and 650,000. The fluid flow was assumed to be air (mimicking the real-life situation in which air is fed to the cathode side of the fuel cell) and some arbitrary values of air velocity and oxygen concentration were used for the boundary conditions. Namely, the velocity was prescribed at the inlet of the domain (0.1 m/s) and the pressure was set at the outlet of the domain (0 Pa). Note that the bulk oxygen diffusivity coefficient D_{O2} at 20 °C and 1 atm is around 0.219 cm^2/s [71]. In addition, it is assumed that the inlet air comprises 21% oxygen and 79% nitrogen. As for the conservation of the species, the inlet oxygen concentration, $C_{in,O2}$, is 8.73 mol/m^3 and the outlet oxygen concentration is 7.73 mol/m^3. It has been shown in the supplementary material how the inlet concentration of oxygen has been calculated. The governing equations (2) and (3) were solved independently for each direction (i.e. through-plane direction (Fig. 3a) and in-plane direction (Fig. 3b)) to respectively solve for the distributions of velocity and oxygen concentration within the computational domain and subsequently estimate the gas permeability and effective diffusivity for each principal direction. It is noteworthy that the convective term is not considered in Equation (3) as the objective is to estimate the effective diffusivity of the porous media and for this to be achieved, one only needs to solve for the concentration, and not the velocities. It should be noted that symmetry boundary conditions were used for the left and the right sides (through-plane case) and wall boundary conditions were used for top and bottom sides (in-plane case). The solid-phase within the domains (Fig. 3) are the white areas and the no-slip boundary conditions were used for the walls of these areas. The simulations were performed assuming that the temperature of the inlet is 20 °C. The models were numerically solved using a small workstation (Inter® Xenon® CPU E3-1246 v3@ 3.50 GHz, 16 GB installed RAM) and the computational time for each modelled slice was found to be between 140 and 220s. The estimated properties using the above workflow (i.e. imaging, image processing and numerical modelling) have been presented and discussed. Figure S1 in the supplementary material is a flow chart that schematically shows the methodology and the order of the investigations.

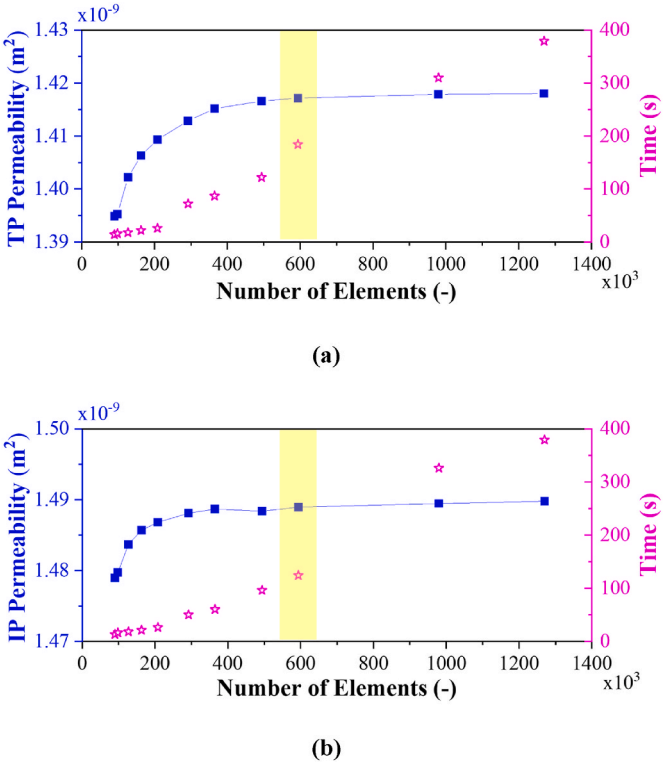

Fig. 2. Change of through-plane (a) and in-plane (b) permeability (and the corresponding computation time) of the 200th slice with number of elements. Yellow strip shows the selected number of elements which is around 600,000.

2.3. Structural properties

2.3.1. Porosity

The porosity (ε) is the ratio between the void volume and the total volume of the porous medium. All the transport properties of the porous media are a strong function of the porosity. For example, the mass transport properties (e.g. gas permeability and diffusivity) increase with increasing porosity while the electrical and thermal conductivity decrease with increasing porosity [72]. The porosity values are often determined using mercury intrusion porosimetry (MIP) or other standard porosimetry methods. The maximum reported value for the porosity of a commercially available carbon fibre-based GDL is 0.9 while the porosity of nickel foam could be as high as 0.98 [3,73,74], signalling higher transport properties of the latter structure (i.e. the nickel foam). The porosity of the nickel foam sample was estimated for each imaged slice by using the COMSOL Multiphysics® 5.5 to measure the void phases and solid phases. The porosity of the nickel foam sample was estimated for each imaged slice within the Geometry node of the COMSOL Multiphysics® 5.5 by separately measuring the areas for each of the void and the solid phases. Evidently, the porosity for each slice is estimated by dividing the area of the void by the total area (which is the sum of the void and solid phases [75]:

$$\varepsilon = \frac{Void\ phases}{Total\ phases} \tag{4}$$

2.3.2. Tortuosity

The tortuosity (τ) is, as implied by its name, a measure of how tortuous is the pathway for the transported fluid; the higher is the tortuosity, the longer is the pathway for the fluid. It also provides insight into the interconnections between the pores of the porous media. The following Equations (5) and (6) (which were found to be suitable for two-dimensional domains) could be (and have been in this work) used to estimate the tortuosity values [70,76]:

$$\tau_{TP} = \frac{u_{mag}}{u_y} \tag{5}$$

$$\tau_{IP} = \frac{u_{mag}}{u_x} \tag{6}$$

where u_{mag} is the velocity magnitude averaged over the computational domain and u_y and u_x are, respectively, the velocity components in the through- and in-plane directions, averaged over the computational domain.

2.3.3. Pore size distribution

The "pore" term means a small void/space/perforation that connects the cells. The pore size distribution strongly impacts on the transport of reactant gases and liquid water within the GDLs, particularly those at the cathode side, and subsequently impacts the performance of the fuel cell [19,41]. The pore size distribution was estimated for the selected imaged 20 slices using an open-source ImageJ/Fiji software package [77]. All the pores are manually measured and counted through the slices using ImageJ/Fiji software and the pore size distributions have been given in Section 3.3. It should be noted that, with SEM images, one could only compute the pore size distribution on the surface of the scanned structure while the X-ray CT enables one to obtain the multiple local interior pore size distribution of the structure.

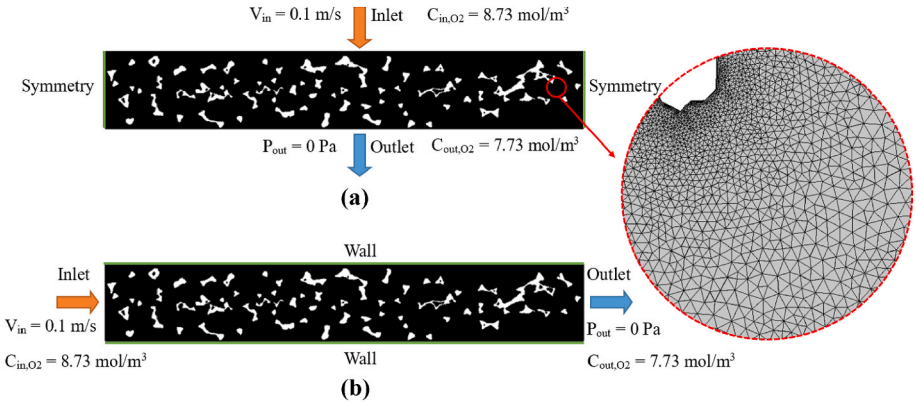

Fig. 3. The meshed computational domain for a typical modelled nickel foam slice, labelled with boundary conditions, when solving the conservation of momentum and conservation of species equations in (a) the through-plane and (b) the in-plane directions. Note that the white areas in the domains represent the solid phase (i.e. the ligaments of the nickel foam).

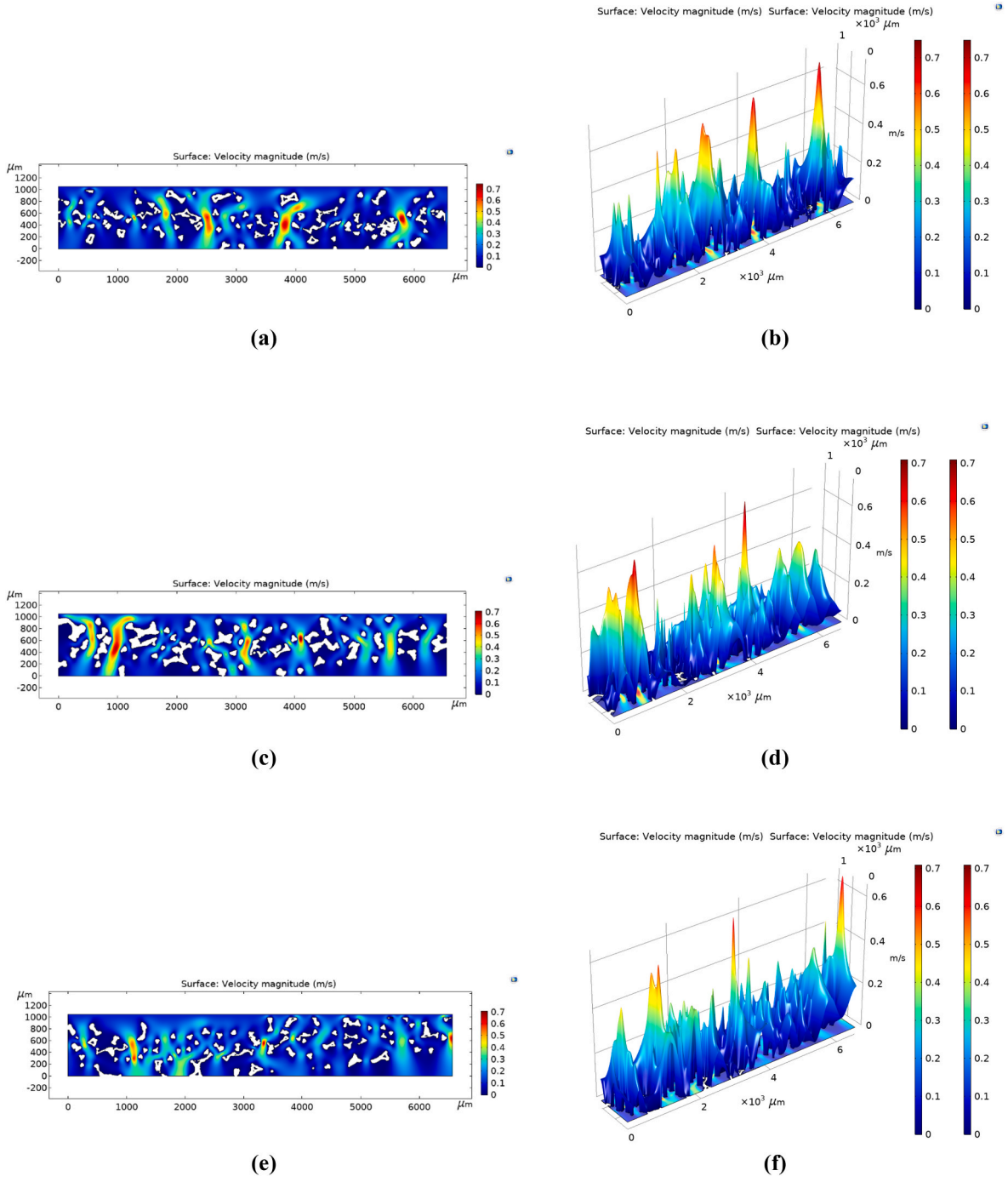

Fig. 4. The numerical-estimated velocity profile for the through-plane flows within the modelled CT nickel foam slice 200 (a and b), 500 (c and d) and 800 (e and f).

2.3.4. *Ligament thickness distribution*

The ligament or the strut is a solid metal rod that forms the cellular structure in the nickel foam. The ligament thickness directly affects the electrical and the thermal conductivity, and the mechanical strength of the nickel foam. As with the pore size distribution, the range of the ligament thickness of the nickel foam and its distribution was determined for the selected imaged 20 slices using an open-source ImageJ/Fiji software [77]. Likewise measuring the pore size, the ligaments have been manually measured and counted through the slices, and the ligament thickness distributions have been presented in Section 3.4.

2.3.5. *Specific surface area*

The specific surface area is the surface area of the material per unit of volume [78]. As with the other above mentioned structural properties, the specific surface area of the nickel foam affects the mass, heat and charge transport distributions [79,80]. The nickel foams inherently possess a very high surface area and this is due to their tetradecahedron structure [81]. The Brunauer Emmett Teller (BET) volumetric and gravimetric methods are often used to measure the specific surface area of porous materials, including the metal foams [82,83]. Further, the knowledge of the porosity and the pore size distribution allows for the estimation of the specific surface area as demonstrated in Refs. [84,85]. The total length of the borders and the area of the solid phase were calculated within COMSOL Multiphysics® 5.5 and when these two quantities are divided, the specific surface area is obtained for the investigated slice.

2.4. Mass transport properties

2.4.1. Gas permeability

The gas permeability is, as implied by the name, a measure how permeable is the porous medium to gases. The low permeability of the GDL leads to higher gas pressure gradients which leads to higher water saturation in the cathode GDLs and potentially undesirable water flooding phenomena particularly at the cathode side [3,18,86–91]. Furthermore, the high gas permeability increases the convective flow, which translates into an increased amount of the reacting gas supplied to the catalyst layer and ultimately better fuel cell performance [8,12,92–98]. Therefore, it is always desirable for the GDL materials to demonstrate high permeability values. For sufficiently low velocities, the viscous resistance is dominant and the inertial resistance is negligible and this enables one to use the simple linear equation of Darcy's Law (rather than the Forchheimer equation) to estimate the permeability of the porous media, K, as follows [93,94,99]:

$$\frac{\Delta P}{L} = \frac{\mu}{K} u \tag{7}$$

where ΔP is the pressure difference across either the thickness (through-plane) or the length (in-plane) of the GDL material(L) and μ is the dynamic viscosity of the flowing fluid. Following the solution of the conservation of the momentum equation, as described in Section 2.2, the pressure drop was computed for each of the 20 modelled nickel foam slices in both the through- and in-plane directions; this enables one to calculate the respective gas permeability values. It should be noted that u has been set to be the velocity prescribed at inlet of the computational domain (i.e. 0.1 m/s). It should be noted that the gas permeability is an intrinsic property of the material and it is therefore invariant with velocity. Figure S2 in the supplementary material show that the pressure gradient changes linearly with the inlet velocity and Figure S3 shows that the gas permeability values (in both directions) for arbitrarily selected CT slices are almost insensitive to the inlet velocity. The through-plane gas permeability of the nickel foam was also experimentally estimated using an in-house setup [8,95] to validate the corresponding computed permeability values. The setup consists of top and bottom fixtures, a flow controller (HFC-202, Teledyne Hastings, UK) and a differential pressure sensor (PX653, Omega, UK). Seven circular samples (25.4 mm in diameter) were punched out of a nickel foam sheet and each sample was placed between the fixtures. Nitrogen gas was passed through the sample and the pressure drop was recorded for each flow rate. Finally, using all the knowledge of all the parameters shown in Equation (7), the gas permeability of each sample was calculated and then the gas permeability values for all the samples were averaged. It should be noted that the dynamic viscosity of nitrogen is 1.751×10^{-5} Pa.s at 20 °C which was the temperature of the room in which the test was conducted [100].

2.4.2. Effective diffusivity

Diffusion is the main mode of transport for the gases in the conventional carbon fibre based GDLs and this is due to their relatively low permeability ($>10^{-13}$ m^2) [96] and is, at least, expected to play a crucial role in transporting the chemical species within the nickel foam based GDLs. The effective diffusivity is a measure on how diffusive the chemical species into each other within the porous medium. The effective diffusivity of the species i into the species j within the GDL,D_{ij}^{eff}, could be estimated using the following form of Fick's law:

$$J = D_{ij}^{eff} \frac{\Delta C}{L} \tag{8}$$

where J is the molar flux (mol/(m^2·s)), and ΔC is the concentration difference between the inlet and outlet across either the thickness (through-plane) or the length (in-plane) of the GDL material (L). The molar flux was, following the solution of the conservation of the chemical species equation as described in Section 2.2, computed for each of the 20 modelled nickel foam slices in both the through- and in-plane directions. With this and with the knowledge of ΔC (1 mol/m^3) and L (1.05 mm for the through-plane direction and 6.65 mm for the in-plane direction), the respective effective diffusivities could be calculated. It should be noted that the species i and j were taken to be oxygen and nitrogen in this study, mimicking the real-life situation in PEFCs where air is typically fed into the cathode of the fuel cell. In addition, it is worth mentioning that the concentration difference does not have an impact on the estimated effective through- or in-plane diffusivity of oxygen as the molar flux proportionally changes with the concentration difference, thus maintaining the proportionality factor (the effective diffusivity of oxygen) constant; see Table S.1, Table S.2 and Figure S.4 in the supplementary material.

3. Results and discussion

Figs. 4 and 5 show the velocity profiles, for the through- and in-plane flow directions, respectively, within one of the modelled CT slices. It is evident that the random position and the size of the ligaments of the foam significantly influence the velocity magnitude and direction within the modelled CT slice, thus resulting in highly non-uniform velocity profiles. Similar profiles were obtained for the other modelled CT slices (not shown). Notably, a slightly more uniform velocity profile is obtained for the in-plane flow compared to the through-plane direction. As will be shown in Section 3.2, this could be attributed to the smaller tortuosity values as demonstrated by the nickel form in the in-plane direction than in the through-plane direction. The following subsections present the computationally-estimated structural and mass transport properties of the nickel foam.

3.1. Porosity

Fig. 6 shows the porosity values for each of the equally-spaced selected 20 slices. The range of the porosity is from 0.844 to 0.873 and the mean values for the porosity values of all the slices is 0.856 with a 95% confidence interval of ±0.003. These porosity values are in agreement with those reported in the literature [101–106]. For instance, the porosity of the nickel foam was experimentally determined by Oun and Kennedy [103] as 0.88. Also, the porosity of the nickel foam was reported by Khayargoli et al. [104] to be between 0.83 and 0.90, and by Slade [107] to be between 0.85 and 0.97. Moreover, Vicente et al. [106] computed the porosity of some nickel foam samples employing 3D CT images and found that it lies between 0.87 and 0.93. These relatively wide ranges for the porosity values and/or the slight discrepancies between the values/ranges reported by the various research groups could be attributed to the potentially different manufacturing settings used [50]. The multiple 2D CT images using computational method, unlike the conventional experimental methods and the 3D numerical X-ray CT studies, reveal how uniform the nickel foam is in terms of porosity. This uniformity and the high values of porosity of nickel foams is expected to facilitate mass transport within the PEFCs.

3.2. Tortuosity

The through- and in-plane tortuosity values for the 20 equally-spaced two-dimensional CT slices are presented in Fig. 7. The average through-plane tortuosity is 1.175, which is between those values reported in the literature by Khayargoli et al. (i.e. 1.15) [104] and Kopanidis et al. (i.e. 1.26) [108]. The average in-plane tortuosity (i.e. 1.124) was found to be slightly less than that in the through-plane direction and in line with those reported in the literature by Brun et al. (i.e. 1.09–1.13) [109]. It is noteworthy that the latter authors estimated the tortuosity making use of the X-ray CT images generated for a nickel foam material. The results shows that the tortuosity of the nickel foam are significantly less than those of the conventionally-used carbon substrates; the smallest

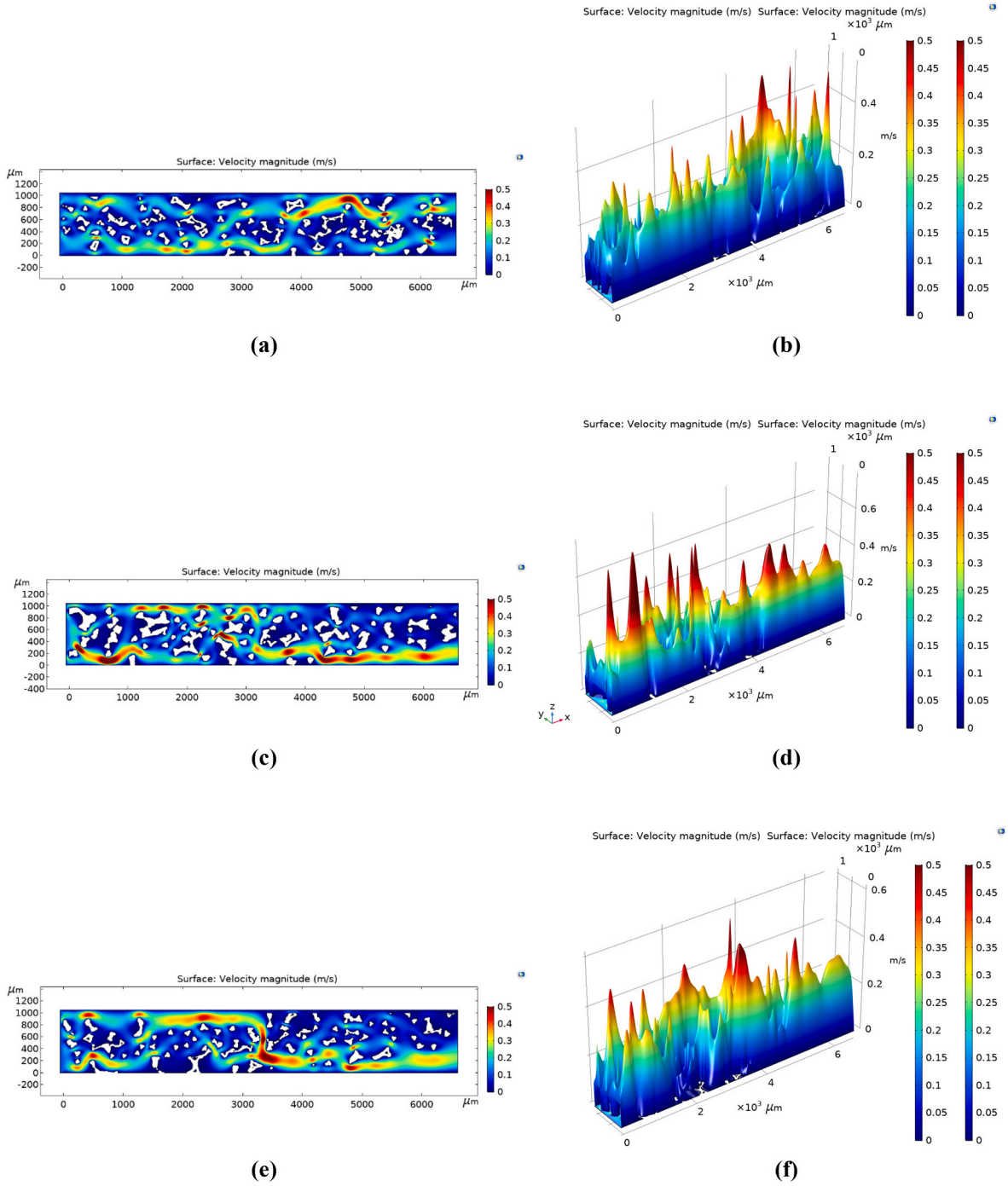

Fig. 5. The numerical-estimated velocity profile for the in-plane flows within the modelled CT nickel foam slice 200 (a and b), 500 (c and d) and 800 (e and f).

reported tortuosity for an SGL and Toray carbon substrates were found to be 1.33 and 2.50, respectively [110,111]. This suggests that, compared to the carbon substrates, the reacting gases and/or excess water would flow through more straight pathways when using nickel foams as the GDLs, thus reducing the mass transport resistance and potentially mitigating the water flooding, particularly beneath the ribs of the flow-field plates.

3.3. Pore size distribution

The pore size distribution histograms for 10 CT slices are shown in Fig. 8. Considering all the slices, the average pore size was calculated to be around 390 (±16) μm and the range of the pore size is between 100 and 750 μm. The above average pore sizes are in line with those reported in the literature. Namely, it lies between that reported by Khayargoli et al. [104], i.e. 360 μm, and that reported by Milazzo et al. [112], Oun and Kennedy [113], and Hellmann et al. [113], i.e. 450 μm. The average pore size of the nickel foam is two orders of magnitude higher than those of the conventional carbon fibre based GDLs [110], which suggests that, as with the tortuosity, that less mass transport resistance is demonstrated by nickel foam based GDLs. It is noteworthy that the nickel foam exhibits a slightly larger pore size compared to other metal foams and this due to the relatively thinner ligament thickness of the former foam [114]. Large pore size in the porous material is beneficial for effective mass transport [115]; Crosnier et al. [116] stated that the larger is the pore diameter, the smaller is the pressure drop and the higher is the

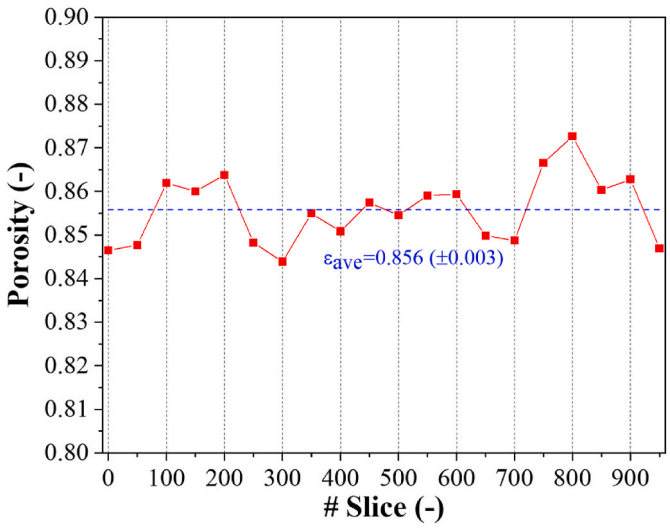

Fig. 6. Computationally computed porosity values for 20 equally-spaced CT nickel foam slices.

permeability. As the pore size of nickel foam decreases, the specific surface area increases which creates an additional flow resistance.

3.4. Ligament thickness distribution

The ligament thickness distribution histograms for 10 CT slices are shown in Fig. 9. Considering all of these 10 slices, the average ligament thickness was calculated to be around 99 (±3) μm and the range of the ligament thickness is between 60 and 180 μm. This calculated average ligament thickness is consistent with those reported in the literature. Namely, Tsolas et al. [117] experimentally and numerically evaluated the properties of nickel foams and reported the ligament thickness as 95 μm. Further, Miwa and Revankar [101] experimentally evaluated the structural characteristics of nickel foam and reported an average ligament thickens that is almost identical to that reported in this study, i.e. ~ 99 μm. It should be noted that the average ligament thickness of nickel is significantly larger than the average carbon fibre thickness of the conventionally used GDLs; the carbon-based GDLs fibre diameter has been reported to be between 7 and 10 μm [118,119].

3.5. Specific surface area

Fig. 10 shows the specific surface area (SSA) for 20 equally-spaced two-dimensional CT slices. As seen from the figure, the range of the SSA is between around 40,500 and 46,100 m^{-1}. The average SSA for all the slices is around 43,560 (±310) m^{-1} which is in accordance with those reported in the literature. Namely, Yang et al. [120] experimentally investigated nickel foam as a cathode electrode for aluminium-hydrogen peroxide fuel cells and they reported the SSA of the nickel foam as 42,800 m^{-1}. Similarly, Langlois and Coeuret [121] experimentally assessed the structural properties of nickel foams and they, using a BET analysis, reported that the SSA of the nickel foam sample to be around 41,000 m^{-1}. Compared to the conventionally used carbon substrates, nickel foam possess significantly higher SSA; this implies that they have superior heat and electrical conduction due to the better contact to the flow-field plates [113].

3.6. Gas permeability

The through- and in-plane permeability was calculated as described in Section 2.4.1 for all the 20 equally-spaced two-dimensional CT slices; see Fig. 11. The average through-plane and in-plane permeability values are, considering the permeability of all the individual modelled slices, 1.26×10^{-9} and 1.39×10^{-9} m^2, respectively. The range is between 9.81×10^{-10} and 1.51×10^{-9} m^2 for the through-plane permeability and is between 8.63×10^{-10} and 1.84×10^{-9} m^2 for the in-plane permeability. The above computationally-estimated through-plane permeability is in very good agreement with those experimentally estimated values using the in-house set-up which is 1.40×10^{-9} m^2. Further, the above average permeabilities are in excellent agreement with those reported in the literature. Namely, Khayargoli et al. [104] and Medraj et al. [122] experimentally estimated the through-plane permeability of nickel foam as 1.30×10^{-9} m^2. The average in-plane permeability computed in this study lies between that reported by Hugo et al. (1.38×10^{-9} m^2) [102] and that reported by Miwa and Revankar (1.45×10^{-9} m^2) [123]. Overall, the gas permeability of nickel foam is at least two orders of magnitudes higher than those of the conventionally used carbon fibre based substrates whose values are normally between 10^{-11} and 10^{-12} m^2 [110]. This signifies that nickel foam based GDL would demonstrate significantly higher convective flows than the conventionally used GDLs, thus improving the supply of the reactant gases to the catalyst layers and/or the removal of excess water from the catalyst layers. Another observation is that the gas permeability of nickel foam was found to be more isotropic than that of

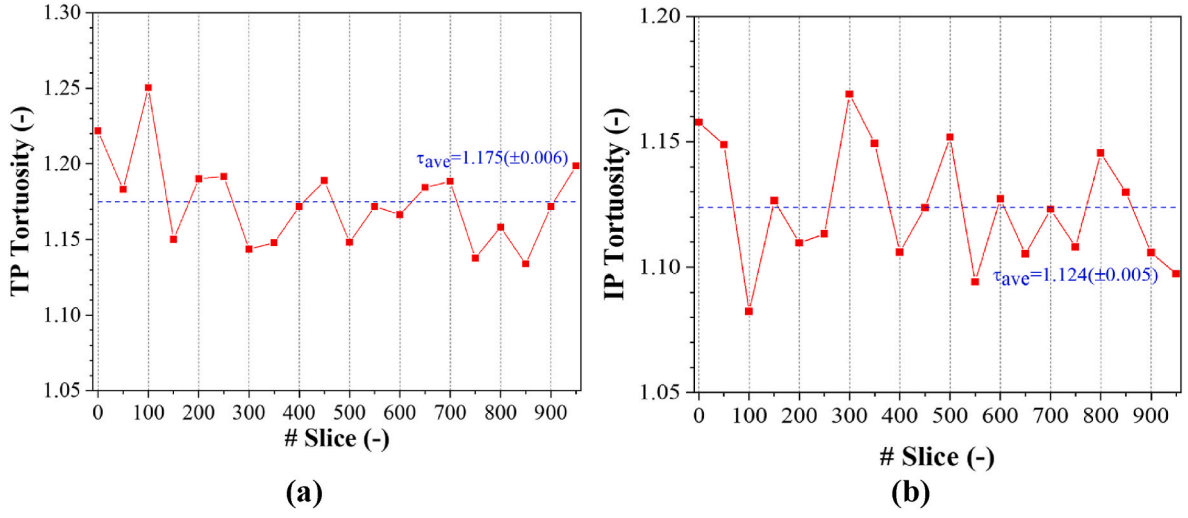

Fig. 7. Computationally computed (a) through-plane tortuosity and (b) in-plane tortuosity for 20 equally-spaced CT nickel foam slices.

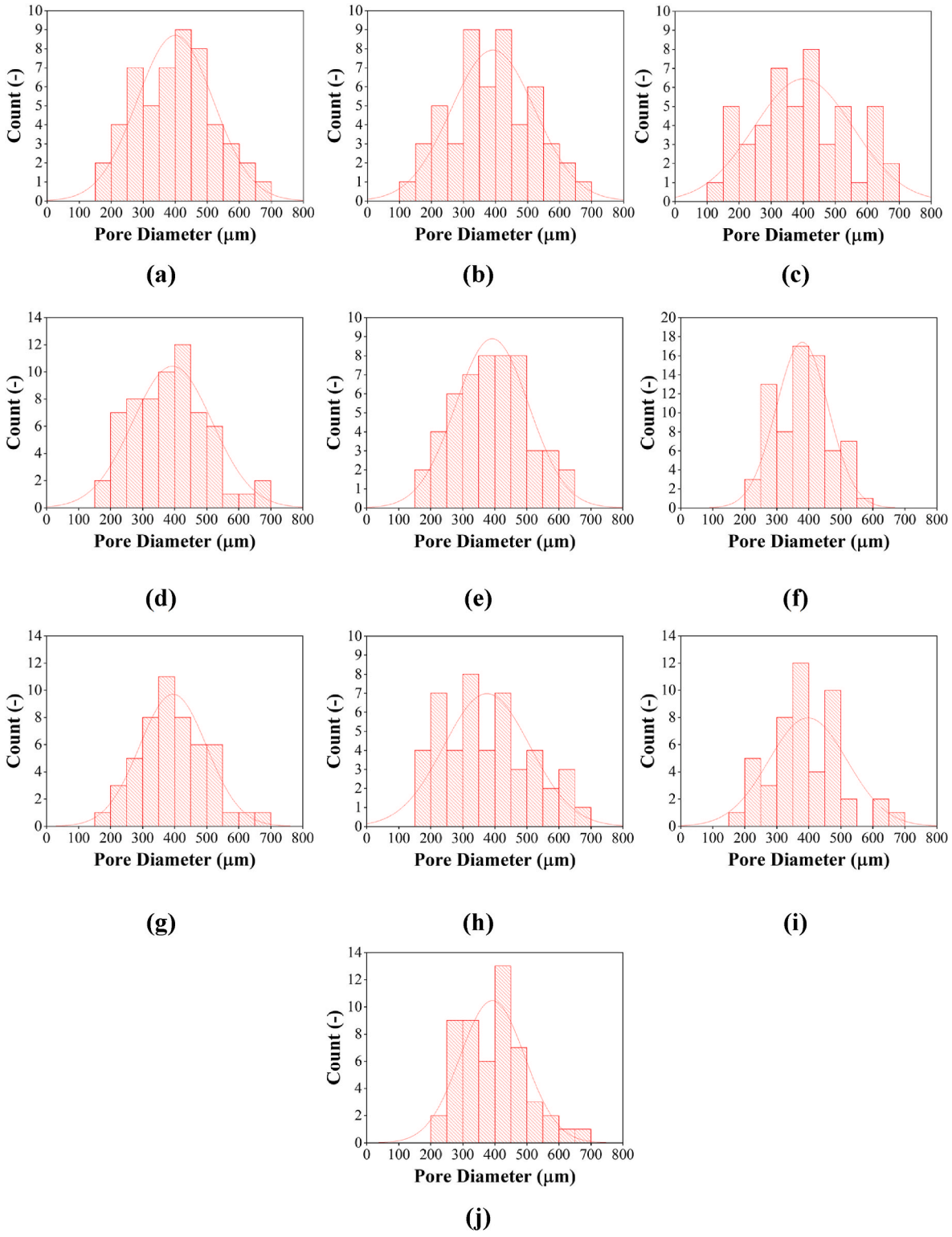

Fig. 8. The pore size distribution for the CT nickel foam slice number: (a) 0, (b) 100, (c) 200, (d) 300, (e) 400, (f) 500, (g) 600, (h) 700, (i) 800, and (j) 900.

the commonly used carbon fibre based carbon substrates; the in-plane permeability of the latter material is larger than the through-plane permeability by almost one order of magnitude [12,124].

3.7. Effective diffusivity

Fig. 12 shows the through- and in-plane effective diffusivity of oxygen into nitrogen corrected for the structure of the nickel foam for the all the 20 equally-spaced two-dimensional CT slices. The average through- and in-plane effective diffusivity are, considering all the 20 CT slices, 0.154 and 0.166 cm^2/s, respectively. The range is between 0.142 and 0.165 cm^2/s for the through-plane effective diffusivity and is between 0.156 and 0.176 cm^2/s for the in-plane effective diffusivity. As with the gas permeability of nickel foam, the effective diffusivity of nickel foam shows a good degree of isotropy as evidenced from the comparable values for the effective diffusivity in the through- and in-plane

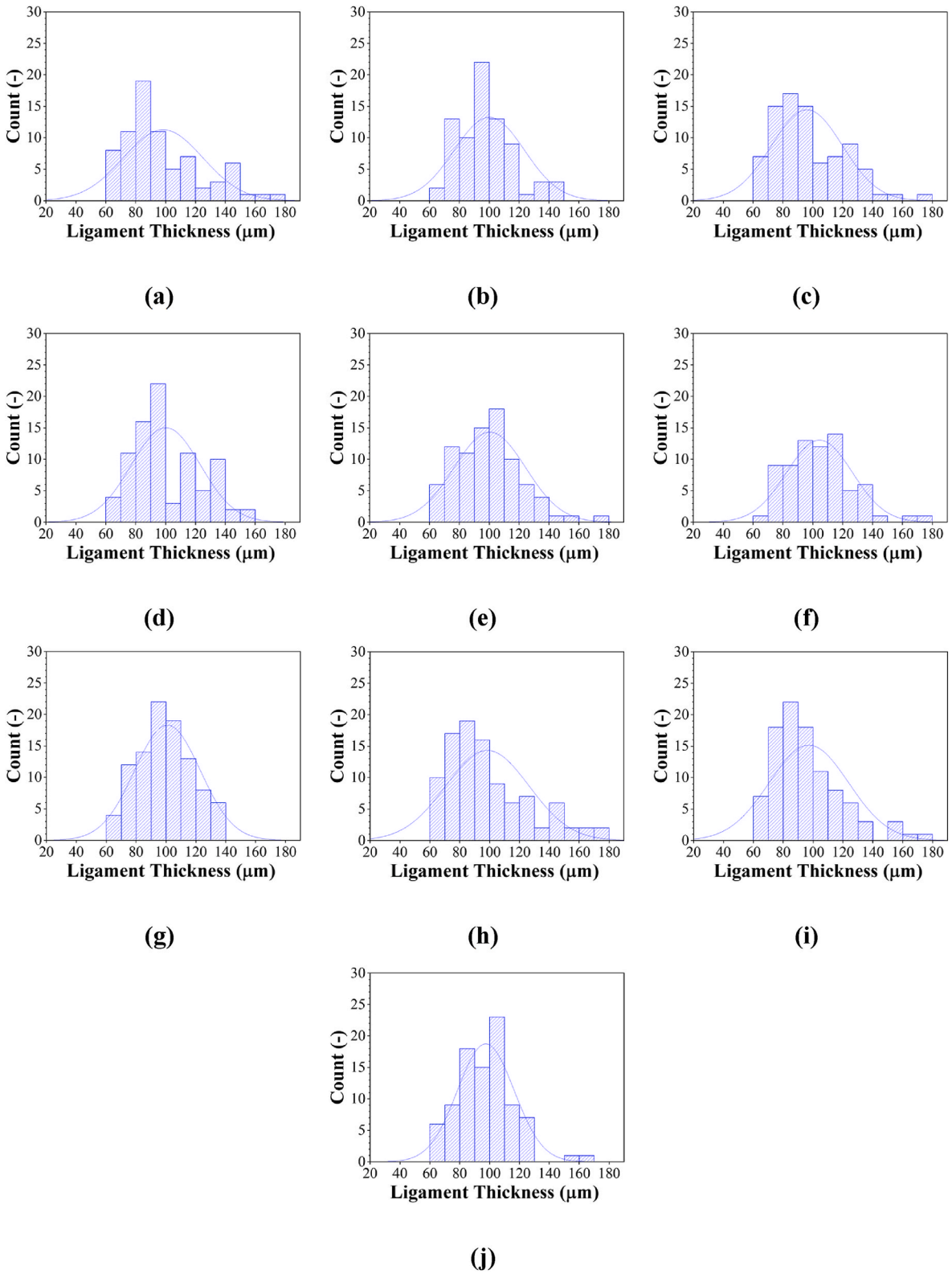

Fig. 9. The ligament thickness distribution for the CT nickel foam slice number: (a) 0, (b) 100, (c) 200, (d) 300, (e) 400, (f) 500, (g) 600, (h) 700, (i) 800, and (j) 900.

directions. This should be compared with the effective diffusivity of the commonly used carbon substrates where the in-plane diffusivity is higher than the through-plane value by a factor of 1.3–3 [61,125]. Moreover, the nickel foam-based GDL yields a much higher effective diffusivity for both the through- and in-plane directions than those of the conventional carbon-based GDLs which are typically between 0.066 and 0.120 cm^2/s (for through-plane direction) and 0.085 and 0.124 cm^2/s (for in-plane direction), respectively [126].

4. Conclusions

Nickel foams have a great potential to be used as gas diffusion layers

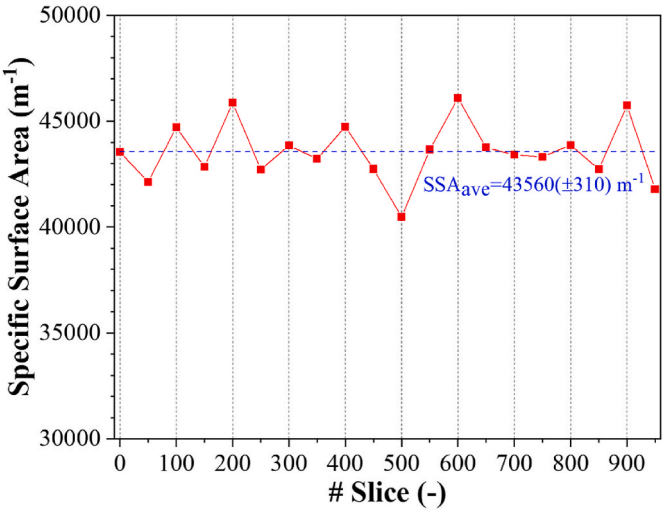

Fig. 10. Computationally computed specific surface area values for 20 equally-spaced CT nickel foam slices.

in polymer electrolyte fuel cells and this is due to their superior structural and transport properties. In this work, some key structural (porosity, tortuosity, pore size distribution, ligament thickness distribution, and specific surface area) and mass transport (gas permeability and effective diffusivity) of a typical nickel foam sample have been determined using equally-spaced multiple computationally-efficient two-dimensional X-ray CT images and/or corresponding numerical models. This is, in addition to saving computational time through not solving computationally expensive three-dimensional images and/or numerical models, performed to check for the multidimensional uniformity of the nickel foam samples. The main findings could be summarised as follows:

- All the computationally-determined properties of the nickel foam, compared to those of the conventionally-used carbon substrates, demonstrate better uniformity in the in-plane and through-plane directions and better isotropy as evidenced from the comparable individual values computed for all the two-dimensional CT slices. Further, all of these computed properties were found to be in agreement with experimental and/or computationally-determined literature data.
- The mean porosity and the mean pore size of the nickel foam sample were computed to be around 0.86 and 390 μm respectively; these

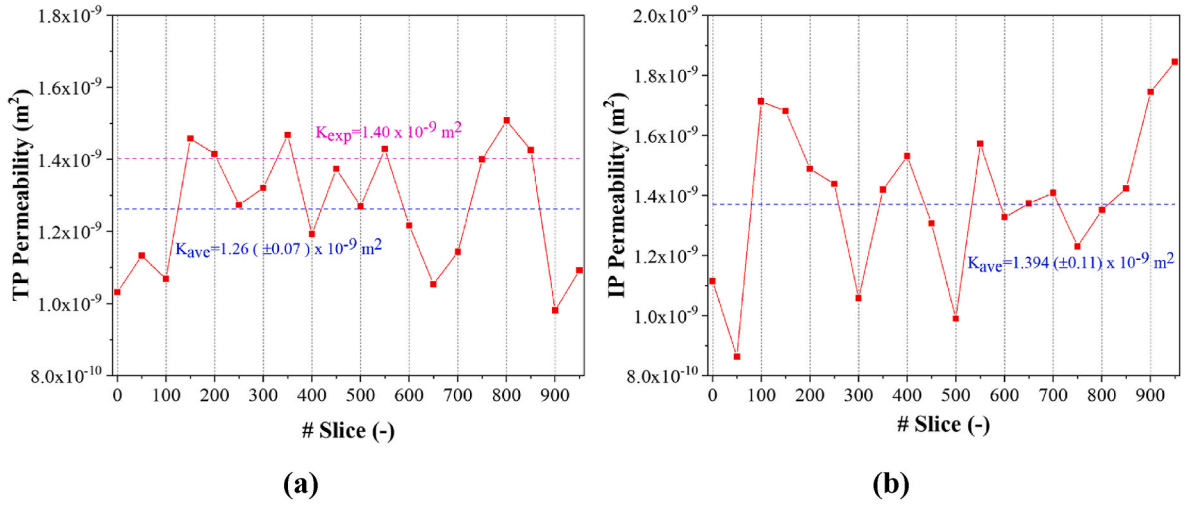

Fig. 11. Computationally computed (a) through-plane and (b) in-plane gas permeability for 20 equally-spaced CT nickel foam slices.

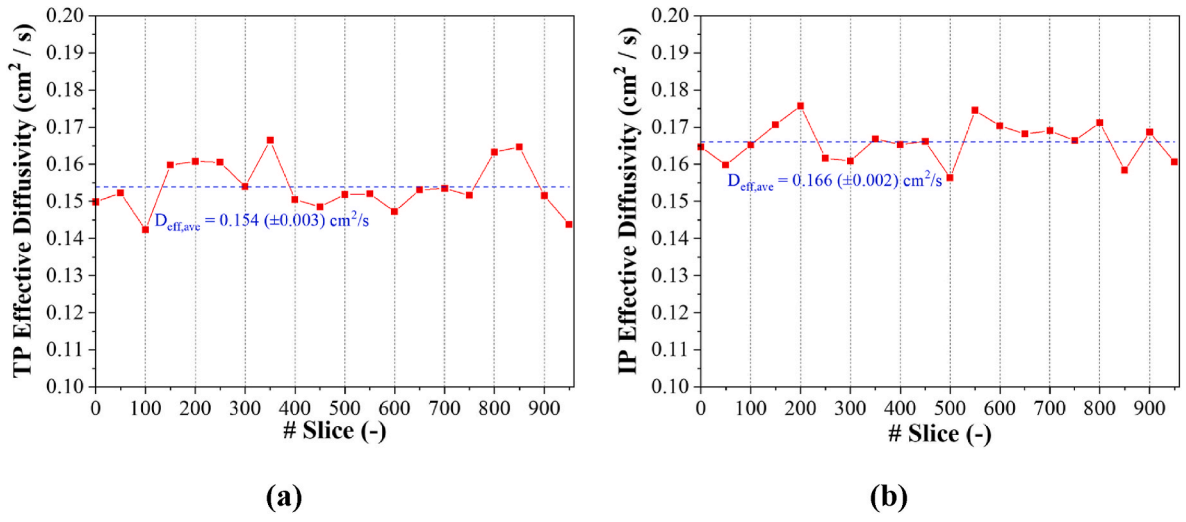

Fig. 12. Computationally computed (a) through-plane and (b) in-plane effective diffusivity of oxygen into nitrogen for 20 equally-spaced CT nickel foam slices.

values are, compared to those of the conventionally-used carbon substrates, high; thus facilitating the mass transport of the gases and liquid water to/from the catalysts layers. Likewise, the relatively low through-plane (~1.18) and in-plane (~1.12) tortuosity lowers the mass transport resistance of the chemical species.

- The mean ligament thickness was computed to be around 99 μm which is one order of magnitude higher than the mean carbon fibre diameter of the conventionally-used carbon substrates; thus implying better mechanical support by nickel foam for the delicate membrane electrode assembly of the fuel cell.
- The computed mean through-plane (1.26×10^{-9} m^2) and in-plane (1.39×10^{-9} m^2) gas permeability was found to be at least one order of magnitude higher than those of the normally-used carbon substrates, signifying higher contribution of convective flow to the mass transport of gases within the nickel foam based GDL. Likewise, the computed mean effective through-plane (0.154 cm^2/s) and in-plane (0.166 cm^2/s) gas diffusivity was found to be higher than those of the carbon substrates by an order of magnitude, meaning more effective diffusive transport to/from the catalyst layer and beneath the ribs of the flow field plates.

Authors Statement

Mustafa Ercelik: Conceptualization, Methodology, Software, Formal analysis, Investigation, Validation, Writing – original draft, Writing – review & editing, Visualization. Mohammed S. Ismail: Conceptualization, Methodology, Software, Formal analysis, Investigation, Validation, Writing – review & editing, Supervision. Derek B. Ingham: Supervision, Writing – review & editing. Kevin J. Hughes: Supervision, Writing – review & editing. Lin Ma: Supervision, Writing – review & editing. Mohamed Pourkashanian: Supervision, Writing – review & editing, Project administration.

Declaration of competing interest

The authors declare that they have no known competing financial interests or personal relationships that could have appeared to influence the work reported in this paper.

Data availability

The authors do not have permission to share data.

Acknowledgements

The first author, Mustafa Ercelik, would like to thank the Republic of Turkey Ministry of National Education for the financial support during his PhD studies.

Nomenclature

Symbols

C	Concentration (mol/m^3)
ΔC	Concentration difference (mol/m^3)
D	Diffusion coefficient (cm^2/s)
D_{O2}	Bulk oxygen diffusivity into nitrogen (cm^2/s)
D_{ij}^{eff}	Effective diffusivity of the species *i* into species *j* (cm^2/s)
I	Identity matrix
J	Molar flux ($mol/(m^2\text{-}s)$)
K	Permeability (m^2)
L	Length (mm)
P	Pressure (Pa)
ΔP	Pressure difference (Pa)
R	Sink source
u	Fluid velocity (m/s)
u_{mag}	Velocity magnitude (m/s)
u_x	Velocity in through-plane direction (m/s)
u_y	Velocity in in-plane direction (m/s)

Greek symbols

ε	Porosity (−)
μ	Dynamic Viscosity of fluid (Pa·s)
ρ	Fluid density (kg/m^3)
τ	Tortuosity (−)

Abbreviations

BET	Brunauer–Emmett–Teller
CT	Computed tomography
FFP	Flow field plate
GDL	Gas diffusion layer
MIP	Mercury intrusion porosimetry
ORR	Oxygen reduction reaction
PEFC	Polymer electrolyte fuel cell
SEM	Scanning electron microscopy
SSA	Specific surface area (m^{-1})

Subscripts & superscripts

ave	Average
eff	Effective
exp	Experimental
i,j	the species i into species j
in	Inlet
IP	In-plane
mag	Magnitude
out	Outlet
O_2	Oxygen
TP	Through-plane
x	x-direction
y	y-direction

Appendix A. Supplementary data

Supplementary data to this article can be found online at https://doi.org/10.1016/j.energy.2022.125531.

References

[1] Tanaka S, Bradfield WW, Legrand C, Malan AG. Numerical and experimental study of the effects of the electrical resistance and diffusivity under clamping pressure on the performance of a metallic gas-diffusion layer in polymer electrolyte fuel cells. J Power Sources 2016;330:273–84. https://doi.org/10.1016/j.jpowsour.2016.08.121.

[2] Barbir F. Front Matter. Biochem Heal Prof 2012. https://doi.org/10.1016/b978-0-7295-3874-9.50001-8. iii.

[3] Ozden A, Shahgaldi S, Li X, Hamdullahpur F. A review of gas diffusion layers for proton exchange membrane fuel cells—with a focus on characteristics, characterization techniques, materials and designs. Prog Energy Combust Sci 2019;74:50–102. https://doi.org/10.1016/j.pecs.2019.05.002.

[4] Wilberforce T, El-Hassan Z, Khatib FN, Al Makky A, Baroutaji A, Carton JG, et al. Developments of electric cars and fuel cell hydrogen electric cars. Int J Hydrogen Energy 2017;42:25695–734. https://doi.org/10.1016/j.ijhydene.2017.07.054.

[5] Alaefour I, Shahgaldi S, Ozden A, Li X, Hamdullahpur F. The role of flow-field layout on the conditioning of a proton exchange membrane fuel cell. Fuel 2018;230:98–103. https://doi.org/10.1016/j.fuel.2018.05.062.

[6] Carton JG, Olabi AG. Design of experiment study of the parameters that affect performance of three flow plate configurations of a proton exchange membrane fuel cell. Energy 2010;35:2796–806. https://doi.org/10.1016/j.energy.2010.02.044.

[7] Ismail MS, Borman D, Damjanovic T, Ingham DB, Pourkashanian M. On the through-plane permeability of microporous layer-coated gas diffusion layers used in proton exchange membrane fuel cells. Int J Hydrogen Energy 2011;36:10392–402. https://doi.org/10.1016/j.ijhydene.2010.09.012.

[8] Aldakheel F, Ismail MS, Hughes KJ, Ingham DB, Ma L, Pourkashanian M, et al. Gas permeability, wettability and morphology of gas diffusion layers before and after performing a realistic ex-situ compression test. Renew Energy 2020;151:1082–91. https://doi.org/10.1016/j.renene.2019.11.109.

[9] Hasanpour S, Hoorfar M, Phillion AB. Different methods for determining porosity of gas diffusion layer using X-ray microtomography. Electrochim Acta 2015;185:34–9. https://doi.org/10.1016/j.electacta.2015.10.083.

[10] Dhanushkodi SR, Capitanio F, Biggs T, Mérida W. Understanding flexural, mechanical and physico-chemical properties of gas diffusion layers for polymer membrane fuel cell and electrolyzer systems. Int J Hydrogen Energy 2015;40:16846–59. https://doi.org/10.1016/j.ijhydene.2015.07.033.

[11] Rama P, Liu Y, Chen R, Ostadi H, Jiang K, Gao Y, et al. A numerical study of structural change and anisotropic permeability in compressed carbon cloth polymer electrolyte fuel cell gas diffusion layers. Fuel Cell 2011;11:274–85. https://doi.org/10.1002/fuce.201000037.

[12] Ismail MS, Damjanovic T, Hughes K, Ingham DB, Ma L, Pourkashanian M, et al. Through-plane permeability for untreated and PTFE-treated gas diffusion layers in proton exchange membrane fuel cells. J Fuel Cell Sci Technol 2010;7. https://doi.org/10.1115/1.4000685. 0510161–7.

[13] Ijaodola OS, El- Hassan Z, Ogungbemi E, Khatib FN, Wilberforce T, Thompson J, et al. Energy efficiency improvements by investigating the water flooding management on proton exchange membrane fuel cell (PEMFC). Energy 2019;179:246–67. https://doi.org/10.1016/j.energy.2019.04.074.

[14] Rashapov R, Imami F, Gostick JT. A method for measuring in-plane effective diffusivity in thin porous media. Int J Heat Mass Tran 2015;85:367–74. https://doi.org/10.1016/j.ijheatmasstransfer.2015.01.101.

[15] Ogungbemi E, Ijaodola O, Khatib FN, Wilberforce T, El Hassan Z, Thompson J, et al. Fuel cell membranes – pros and cons. Energy 2019;172:155–72. https://doi.org/10.1016/j.energy.2019.01.034.

[16] Carton JG, Olabi AG. Three-dimensional proton exchange membrane fuel cell model: comparison of double channel and open pore cellular foam flow plates. Energy 2017;136:185–95. https://doi.org/10.1016/j.energy.2016.02.010.

[17] Wang Y, Wang CY, Chen KS. Elucidating differences between carbon paper and carbon cloth in polymer electrolyte fuel cells. Electrochim Acta 2007;52:3965–75. https://doi.org/10.1016/j.electacta.2006.11.012.

[18] Han M, Xu JH, Chan SH, Jiang SP. Characterization of gas diffusion layers for PEMFC. Electrochim Acta 2008;53:5361–7. https://doi.org/10.1016/j.electacta.2008.02.057.

[19] Jayakumar A, Sethu SP, Ramos M, Robertson J, Al-Jumaily A. A technical review on gas diffusion, mechanism and medium of PEM fuel cell. Ionics 2015;21:1–18. https://doi.org/10.1007/s11581-014-1322-x.

[20] Singh Y, White RT, Najm M, Haddow T, Pan V, Orfino FP, et al. Tracking the evolution of mechanical degradation in fuel cell membranes using 4D in situ visualization. J Power Sources 2019;412:224–37. https://doi.org/10.1016/j.jpowsour.2018.11.049.

[21] Park J, Oh H, Ha T, Lee Y Il, Min K. A review of the gas diffusion layer in proton exchange membrane fuel cells: durability and degradation. Appl Energy 2015;155:866–80. https://doi.org/10.1016/j.apenergy.2015.06.068.

[22] Wu J, Yuan XZ, Martin JJ, Wang H, Zhang J, Shen J, et al. A review of PEM fuel cell durability: degradation mechanisms and mitigation strategies. J Power Sources 2008;184:104–19. https://doi.org/10.1016/j.jpowsour.2008.06.006.

[23] Dukhan N. Correlations for the pressure drop for flow through metal foam. Exp Fluid 2006;41:665–72. https://doi.org/10.1007/s00348-006-0194-x.

[24] Dukhan N, Ali M. Effect of confining wall on properties of gas flow through metal foam: an experimental study, vol. 91. Transp Porous Media; 2012. p. 225–37. https://doi.org/10.1007/s11242-011-9841-7.

[25] Dukhan N, Patel K. Effect of sample's length on flow properties of open-cell metal foam and pressure-drop correlations. J Porous Mater 2011;18:655–65. https://doi.org/10.1007/s10934-010-9423-z.

[26] Hmad AA, Dukhan N. Cooling design for pem fuel-cell stacks employing air and metal foam: simulation and experiment. Energies 2021;14. https://doi.org/10.3390/en14092687.

[27] Wang Y, Leung DYC, Xuan J, Wang H. A review on unitized regenerative fuel cell technologies, part B: unitized regenerative alkaline fuel cell, solid oxide fuel cell, and microfluidic fuel cell. Renew Sustain Energy Rev 2017;75:775–95. https://doi.org/10.1016/j.rser.2016.11.054.

[28] Mukanova A, Nurpeissova A, Urazbayev A, Kim SS, Myronov M, Bakenov Z. Silicon thin film on graphene coated nickel foam as an anode for Li-ion batteries. Electrochim Acta 2017;258:800–6. https://doi.org/10.1016/j.electacta.2017.11.129.

[29] Majasan JO, Iacoviello F, Cho JIS, Maier M, Lu X, Neville TP, et al. Correlative study of microstructure and performance for porous transport layers in polymer electrolyte membrane water electrolysers by X-ray computed tomography and electrochemical characterization. Int J Hydrogen Energy 2019;44:19519–32. https://doi.org/10.1016/j.ijhydene.2019.05.222.

[30] Rybár R, Beer M, Kudelas D, Pandula B. Copper metal foam as an essential construction element of innovative heat exchanger. Metalurgija 2016;55:489–92.

[31] Liang L, Diao YH, Zhao YH, Wang ZY, Bai FW. Numerical and experimental investigations of latent thermal energy storage device based on a flat micro-heat pipe array–metal foam composite structure. Renew Energy 2020;161:1195–208. https://doi.org/10.1016/j.renene.2020.07.033.

[32] Toghyani S, Afshari E, Baniasadi E. Metal foams as flow distributors in comparison with serpentine and parallel flow fields in proton exchange membrane electrolyzer cells. Electrochim Acta 2018;290:506–19. https://doi.org/10.1016/j.electacta.2018.09.106.

[33] Tan WC, Saw LH, Thiam HS, Xuan J, Cai Z, Yew MC. Overview of porous media/metal foam application in fuel cells and solar power systems. Renew Sustain Energy Rev 2018;96:181–97. https://doi.org/10.1016/j.rser.2018.07.032.

[34] Sim Y, Kwak J, Kim SY, Jo Y, Kim S, Kim SY, et al. Formation of 3D graphene-Ni foam heterostructures with enhanced performance and durability for bipolar plates in a polymer electrolyte membrane fuel cell. J Mater Chem 2018;6:1504–12. https://doi.org/10.1039/c7ta07598g.

[35] Tseng CJ, Tsai BT, Liu ZS, Cheng TC, Chang WC, Lo SK. A PEM fuel cell with metal foam as flow distributor. Energy Convers Manag 2012;62:14–21. https://doi.org/10.1016/j.enconman.2012.03.018.
[36] Sajid Hossain M, Shabani B. Metal foams application to enhance cooling of open cathode polymer electrolyte membrane fuel cells. J Power Sources 2015;295:275–91. https://doi.org/10.1016/j.jpowsour.2015.07.022.
[37] Tabe Y, Nasu T, Morioka S, Chikahisa T. Performance characteristics and internal phenomena of polymer electrolyte membrane fuel cell with porous flow field. J Power Sources 2013;238:21–8. https://doi.org/10.1016/j.jpowsour.2013.03.047.
[38] Tseng CJ, Heush YJ, Chiang CJ, Lee YH, Lee KR. Application of metal foams to high temperature PEM fuel cells. Int J Hydrogen Energy 2016;41:16196–204. https://doi.org/10.1016/j.ijhydene.2016.06.149.
[39] Tsai BT, Tseng CJ, Liu ZS, Wang CH, Lee CI, Yang CC, et al. Effects of flow field design on the performance of a PEM fuel cell with metal foam as the flow distributor. Int J Hydrogen Energy 2012;37:13060–6. https://doi.org/10.1016/j.ijhydene.2012.05.008.
[40] Baroutaji A, Carton JG, Stokes J, Olabi AG. Application of open pore cellular foam for air breathing PEM fuel cell. Int J Hydrogen Energy 2017;42:25630–8. https://doi.org/10.1016/j.ijhydene.2017.05.114.
[41] Shin DK, Yoo JH, Kang DG, Kim MS. Effect of cell size in metal foam inserted to the air channel of polymer electrolyte membrane fuel cell for high performance. Renew Energy 2018;115:663–75. https://doi.org/10.1016/j.renene.2017.08.085.
[42] Liu R, Zhou W, Li S, Li F, Ling W. Performance improvement of proton exchange membrane fuel cells with compressed nickel foam as flow field structure. Int J Hydrogen Energy 2020;45:17833–43. https://doi.org/10.1016/j.ijhydene.2020.04.238.
[43] Zamel N, Li X. Effective transport properties for polymer electrolyte membrane fuel cells - with a focus on the gas diffusion layer. Prog Energy Combust Sci 2013;39:111–46. https://doi.org/10.1016/j.pecs.2012.07.002.
[44] Jung S, Sabharwal M, Jarauta A, Wei F, Gingras M, Gostick J, et al. Estimation of relative transport properties in porous transport layers using pore-scale and pore-network simulations. J Electrochem Soc 2021;168:064501. https://doi.org/10.1149/1945-7111/ac03f2.
[45] Fishman Z, Hinebaugh J, Bazylak A. Microscale tomography investigations of heterogeneous porosity distributions of PEMFC GDLs. J Electrochem Soc 2010;157:1643–50. https://doi.org/10.1149/1.3481443.
[46] Zenyuk IV, Parkinson DY, Connolly LG, Weber AZ. Gas-diffusion-layer structural properties under compression via X-ray tomography. J Power Sources 2016;328:364–76. https://doi.org/10.1016/j.jpowsour.2016.08.020.
[47] Chevalier S, Lavielle N, Hatton BD, Bazylak A. Novel electrospun gas diffusion layers for polymer electrolyte membrane fuel cells: Part I. Fabrication, morphological characterization, and in situ performance. J Power Sources 2017;352:272–80. https://doi.org/10.1016/j.jpowsour.2017.03.098.
[48] Obermaier M, Bauer A, Dalkilic M, Rauber M, Scheu C. Gas diffusion layer wettability determination by cyclic voltammetry for automotive fuel cells. Fuel Cell 2021:221–33. https://doi.org/10.1002/fuce.202000184.
[49] Kaushal S, Sahu AK, Rani M, Dhakate SR. Multiwall carbon nanotubes tailored porous carbon fiber paper-based gas diffusion layer performance in polymer electrolyte membrane fuel cell. Renew Energy 2019;142:604–11. https://doi.org/10.1016/j.renene.2019.04.096.
[50] Çeçen A, Wargo EA, Hanna AC, Turner DM, Kalidindi SR, Kumbur EC. 3-D microstructure analysis of fuel cell materials: spatial distributions of tortuosity, void size and diffusivity. J Electrochem Soc 2012;159:B299–307. https://doi.org/10.1149/2.068203jes.
[51] De Chiffre L, Carmignato S, Kruth JP, Schmitt R, Weckenmann A. Industrial applications of computed tomography. CIRP Ann - Manuf Technol 2014;63:655–77. https://doi.org/10.1016/j.cirp.2014.05.011.
[52] Vásárhelyi L, Kónya Z, Kukovecz Vajtai R. Microcomputed tomography–based characterization of advanced materials: a review. Mater Today Adv 2020;8:1–13. https://doi.org/10.1016/j.mtadv.2020.100084.
[53] Banerjee R, Hinebaugh J, Liu H, Yip R, Ge N, Bazylak A. Heterogeneous porosity distributions of polymer electrolyte membrane fuel cell gas diffusion layer materials with rib-channel compression. Int J Hydrogen Energy 2016;41:14885–96. https://doi.org/10.1016/j.ijhydene.2016.06.147.
[54] Zenyuk IV, Parkinson DY, Connolly LG, Weber AZ. Gas-diffusion-layer structural properties under compression via X-ray tomography. J Power Sources 2016;328:364–76. https://doi.org/10.1016/j.jpowsour.2016.08.020.
[55] Fishman Z, Bazylak A. Heterogeneous through-plane porosity distributions for treated PEMFC GDLs I. PTFE effect. J Electrochem Soc 2011;158:B841. https://doi.org/10.1149/1.3594578.
[56] Fishman Z, Bazylak A. Heterogeneous through-plane porosity distributions for treated PEMFC GDLs. II. Effect of MPL cracks. J Electrochem Soc 2011;158:B846. https://doi.org/10.1149/1.3594636.
[57] James JP, Choi HW, Pharoah JG. X-ray computed tomography reconstruction and analysis of polymer electrolyte membrane fuel cell porous transport layers. Int J Hydrogen Energy 2012;37:18216–30. https://doi.org/10.1016/j.ijhydene.2012.08.077.
[58] Meyer Q, Ashton S, Boillat P, Cochet M, Engebretsen E, Finegan DP, et al. Effect of gas diffusion layer properties on water distribution across air-cooled, open-cathode polymer electrolyte fuel cells: a combined ex-situ X-ray tomography and in-operando neutron imaging study. Electrochim Acta 2016;211:478–87. https://doi.org/10.1016/j.electacta.2016.06.068.
[59] Meyer Q, Mansor N, Iacoviello F, Cullen PL, Jervis R, Finegan D, et al. Investigation of hot pressed polymer electrolyte fuel cell assemblies via X-ray computed tomography. Electrochim Acta 2017;242:125–36. https://doi.org/10.1016/j.electacta.2017.05.028.
[60] Fazeli M, Hinebaugh J, Fishman Z, Tötzke C, Lehnert W, Manke I, et al. Pore network modeling to explore the effects of compression on multiphase transport in polymer electrolyte membrane fuel cell gas diffusion layers. J Power Sources 2016;335:162–71. https://doi.org/10.1016/j.jpowsour.2016.10.039.
[61] García-Salaberri PA, Zenyuk IV, Shum AD, Hwang G, Vera M, Weber AZ, et al. Analysis of representative elementary volume and through-plane regional characteristics of carbon-fiber papers: diffusivity, permeability and electrical/thermal conductivity. Int J Heat Mass Tran 2018;127:687–703. https://doi.org/10.1016/j.ijheatmasstransfer.2018.07.030.
[62] Fly A, Butcher D, Meyer Q, Whiteley M, Spencer A, Kim C, et al. Characterisation of the diffusion properties of metal foam hybrid flow-fields for fuel cells using optical flow visualisation and X-ray computed tomography. J Power Sources 2018;395:171–8. https://doi.org/10.1016/j.jpowsour.2018.05.070.
[63] Fly A, Meyer Q, Whiteley M, Iacoviello F, Neville T, Shearing PR, et al. X-ray tomography and modelling study on the mechanical behaviour and performance of metal foam flow-fields for polymer electrolyte fuel cells. Int J Hydrogen Energy 2019;44:7583–95. https://doi.org/10.1016/j.ijhydene.2019.01.206.
[64] Kulkarni N, Meyer Q, Hack J, Jervis R, Iacoviello F, Ronaszegi K, et al. Examining the effect of the secondary flow-field on polymer electrolyte fuel cells using X-ray computed radiography and computational modelling. Int J Hydrogen Energy 2019;44:1139–50. https://doi.org/10.1016/j.ijhydene.2018.11.038.
[65] Wu Y, Cho JIS, Whiteley M, Rasha L, Neville TP, Ziesche R, et al. Characterization of water management in metal foam flow-field based polymer electrolyte fuel cells using in-operando neutron radiography. Int J Hydrogen Energy 2019. https://doi.org/10.1016/j.ijhydene.2019.11.069.
[66] Ranut P, Nobile E, Mancini L. High resolution X-ray microtomography-based CFD simulation for the characterization of flow permeability and effective thermal conductivity of aluminum metal foams. Exp Therm Fluid Sci 2015;67:30–6. https://doi.org/10.1016/j.expthermflusci.2014.10.018.
[67] Gao Y, Zhang X, Rama P, Liu Y, Chen R, Ostadi H, et al. Calculating the anisotropic permeability of porous media using the lattice Boltzmann method and X-ray computed tomography. Transport Porous Media 2012;92:457–72. https://doi.org/10.1007/s11242-011-9914-7.
[68] Ostadi H, Rama P, Liu Y, Chen R, Zhang XX, Jiang K. Influence of threshold variation on determining the properties of a polymer electrolyte fuel cell gas diffusion layer in X-ray nano-tomography. Chem Eng Sci 2010;65:2213–7. https://doi.org/10.1016/j.ces.2009.12.019.
[69] Espinoza M, Sundén B, Andersson M, Yuan J. Analysis of porosity and tortuosity in a 2D selected region of solid oxide fuel cell cathode using the lattice Boltzmann method. ECS Trans 2015;65:59–73. https://doi.org/10.1149/06501.0059ecst.
[70] Espinoza Mayken, Andersson Martin, Jy, Bs. Compress effects on porosity, gas-phase tortuosity, and gas permeability in a simulated PEM gas diffusion layer. *,† Arch Therm 2015;33:23–40. https://doi.org/10.1002/er.
[71] Zamel N, Li X, Becker J, Wiegmann A. Effect of liquid water on transport properties of the gas diffusion layer of polymer electrolyte membrane fuel cells. Int J Hydrogen Energy 2011;36:5466–78. https://doi.org/10.1016/j.ijhydene.2011.01.146.
[72] Kandlikar SG, Garofalo ML, Lu Z. Water management in a PEMFC: water transport mechanism and material degradation in gas diffusion layers. Fuel Cell 2011;11:814–23. https://doi.org/10.1002/fuce.201000172.
[73] Poserin V, Marcuson S, Shu J, Wilkinson DS. CVD technique for Inco nickel foam production. Adv Eng Mater 2004;6:454–9. https://doi.org/10.1002/adem.200405142.
[74] Tamayol A, McGregor F, Bahrami M. Single phase through-plane permeability of carbon paper gas diffusion layers. J Power Sources 2012;204:94–9. https://doi.org/10.1016/j.jpowsour.2011.11.084.
[75] Liu J, Wang Y, Song R. A pore scale flow simulation of reconstructed model based on the micro seepage experiment. Geofluids 2017. https://doi.org/10.1155/2017/7459346. 2017.
[76] Nabovati A, Hinebaugh J, Bazylak A, Amon CH. Effect of porosity heterogeneity on the permeability and tortuosity of gas diffusion layers in polymer electrolyte membrane fuel cells. J Power Sources 2014;248:83–90. https://doi.org/10.1016/j.jpowsour.2013.09.061.
[77] ImageJ/Fiji [n.d], https://imagej.net/software/fiji/.
[78] Wohlleben W, Mielke J, Bianchin A, Ghanem A, Freiberger H, Rauscher H, et al. Reliable nanomaterial classification of powders using the volume-specific surface area method. J Nanoparticle Res 2017;19. https://doi.org/10.1007/s11051-017-3741-x.
[79] Duan DL, Zhang RL, Ding XJ, Li S. Calculation of specific surface area of foam metals using dodecahedron model. Mater Sci Technol 2006;22:1364–8. https://doi.org/10.1179/174328406X111138.
[80] Huo S, Cooper NJ, Smith TL, Park JW, Jiao K. Experimental investigation on PEM fuel cell cold start behavior containing porous metal foam as cathode flow distributor. Appl Energy 2017;203:101–14. https://doi.org/10.1016/j.apenergy.2017.06.028.
[81] August A, Nestler B. About the surface area to volume relations of open cell foams. Eng Res Express 2020;2:15021. https://doi.org/10.1088/2631-8695/ab6ac6.
[82] Ozmat B, Leyda B, Benson B. Thermal applications of open-cell metal foams. Mater Manuf Process 2004;19:839–62. https://doi.org/10.1081/AMP-200030568.
[83] Allioux FM, Merhebi S, Tang J, Idrus-Saidi SA, Abbasi R, Saborio MG, et al. Catalytic metal foam by chemical melting and sintering of liquid metal

nanoparticles. Adv Funct Mater 2020;30:1–13. https://doi.org/10.1002/adfm.201907879.
[84] Liu PS. A new method for calculating the specific surface area of porous metal foams. Phil Mag Lett 2010;90:447–53. https://doi.org/10.1080/09500831003745571.
[85] Chen J, Zhang X, Li C, Zhang X, Ren Y, He J, et al. Calculation method of specific surface area of foam metal based on an ideal tetradecahedron model for lithium ion battery. Int J Photoenergy 2020;2020. https://doi.org/10.1155/2020/2478579.
[86] Okonkwo PC, Otor C. A review of gas diffusion layer properties and water management in proton exchange membrane fuel cell system. Int J Energy Res 2021;45:3780–800. https://doi.org/10.1002/er.6227.
[87] Ahmed DH, Sung HJ, Bae J. Effect of GDL permeability on water and thermal management in PEMFCs-I. Isotropic and anisotropic permeability. Int J Hydrogen Energy 2008;33:3767–85. https://doi.org/10.1016/j.ijhydene.2008.04.024.
[88] Ahmed DH, Sung HJ, Bae J. Effect of GDL permeability on water and thermal management in PEMFCs-II. Clamping force. Int J Hydrogen Energy 2008;33:3786–800. https://doi.org/10.1016/j.ijhydene.2008.04.023.
[89] Cindrella L, Kannan AM, Lin JF, Saminathan K, Ho Y, Lin CW, et al. Gas diffusion layer for proton exchange membrane fuel cells-A review. J Power Sources 2009;194:146–60. https://doi.org/10.1016/j.jpowsour.2009.04.005.
[90] Reshetenko TV, St-Pierre J, Rocheleau R. Effects of local gas diffusion layer gas permeability variations on spatial proton exchange membrane fuel cells performance. J Power Sources 2013;241:597–607. https://doi.org/10.1016/j.jpowsour.2013.04.131.
[91] Williams MV, Kunz HR, Fenton JM. Influence of convection through gas-diffusion layers on limiting current in PEM FCs using a serpentine flow field. J Electrochem Soc 2004;151:A1617. https://doi.org/10.1149/1.1789791.
[92] Gurau V, Bluemle MJ, De Castro ES, Tsou YM, Zawodzinski TA, Mann JA. Characterization of transport properties in gas diffusion layers for proton exchange membrane fuel cells. 2. Absolute permeability. J Power Sources 2007;165:793–802. https://doi.org/10.1016/j.jpowsour.2006.12.068.
[93] Orogbemi OM, Ingham DB, Ismail MS, Hughes KJ, Ma L, Pourkashanian M. On the gas permeability of the microporous layer used in polymer electrolyte fuel cells. J Energy Inst 2018;91:894–901. https://doi.org/10.1016/j.joei.2017.09.006.
[94] Orogbemi OM, Ingham DB, Ismail MS, Hughes KJ, Ma L, Pourkashanian M. Through-plane gas permeability of gas diffusion layers and microporous layer: effects of carbon loading and sintering. J Energy Inst 2018;91:270–8. https://doi.org/10.1016/j.joei.2016.11.008.
[95] Aldakheel F, Ismail MS, Hughes KJ, Ingham DB, Ma L, Pourkashanian M. Effects of compression on mechanical integrity, gas permeability and thermal stability of gas diffusion layers with/without sealing gaskets. Int J Hydrogen Energy 2021;46:22907–19. https://doi.org/10.1016/j.ijhydene.2021.04.087.
[96] Ismail MS, Hughes KJ, Ingham DB, Ma L, Pourkashanian M. Effects of anisotropic permeability and electrical conductivity of gas diffusion layers on the performance of proton exchange membrane fuel cells. Appl Energy 2012;95:50–63. https://doi.org/10.1016/j.apenergy.2012.02.003.
[97] Neehall ND, Ismail MS, Hughes KJ, Pourkashanian M. Effect of composition and structure of gas diffusion layer and microporous layer on the through-plane gas permeability of PEFC porous media. Int J Energy Res 2021;45:20988–1005. https://doi.org/10.1002/er.7158.
[98] Lee FC, Ismail MS, Ingham DB, Hughes KJ, Ma L, Lyth SM, et al. Alternative architectures and materials for PEMFC gas diffusion layers: a review and outlook. Renew Sustain Energy Rev 2022;166:112640. https://doi.org/10.1016/j.rser.2022.112640.
[99] Orogbemi OM, Ingham DB, Ismail MS, Hughes KJ, Ma L, Pourkashanian M. The effects of the composition of microporous layers on the permeability of gas diffusion layers used in polymer electrolyte fuel cells. Int J Hydrogen Energy 2016;41:21345–51. https://doi.org/10.1016/j.ijhydene.2016.09.160.
[100] Holman JP. Heat transfer. tenth ed. McGraw-Hill; 2010.
[101] Miwa S, Revankar ST. Hydrodynamic characterization of nickel metal foameffects of pore structure and permeability. Heat Tran Eng 2012;33:800–8. https://doi.org/10.1080/01457632.2012.646872.
[102] Hugo J-M, Brun E, Topi F. Metal foam effective transport properties. Evaporation, condens heat transf. 2011. https://doi.org/10.5772/21321.
[103] Oun H, Kennedy A. Experimental investigation of pressure-drop characteristics across multi-layer porous metal structures. J Porous Mater 2014;21:1133–41. https://doi.org/10.1007/s10934-014-9863-y.
[104] Khayargoli P, Loya V, Lefebvre LP, Medraj M. The impact of microstructure on the permeability of metal foams. CSME 2004 Forum 2004;2004:220–8.
[105] Brun E, Vicente J, Topin F, Occelli R, Clifton MJ. Microstructure and transport properties of cellular materials: representative volume element. Adv Eng Mater 2009;11:805–10. https://doi.org/10.1002/adem.200900131.
[106] Vicente J, Topin F, Daurelle JV. Open celled material structural properties measurement: from morphology to transport properties. Mater Trans 2006;47:2195–202. https://doi.org/10.2320/matertrans.47.2195.
[107] Slade PG. Electrical contacts: principles and applications. CRC press; 2017.
[108] Kopanidis A, Theodorakakos A, Gavaises E, Bouris D. 3D numerical simulation of flow and conjugate heat transfer through a pore scale model of high porosity open cell metal foam. Int J Heat Mass Tran 2010;53:2539–50. https://doi.org/10.1016/j.ijheatmasstransfer.2009.12.067.
[109] Brun E, Vicente J, Topin F, Occelli R. Geometrical measurement of real foams from 3D images. In: 2007 - proc 5th int conf porous met met foam. MetFoam; 2008. 425–8.
[110] El-Kharouf A, Mason TJ, Brett DJL, Pollet BG. Ex-situ characterisation of gas diffusion layers for proton exchange membrane fuel cells. J Power Sources 2012;218:393–404. https://doi.org/10.1016/j.jpowsour.2012.06.099.
[111] Lamanna JM, Kandlikar SG. Determination of effective water vapor diffusion coefficient in pemfc gas diffusion layers. Int J Hydrogen Energy 2011;36:5021–9. https://doi.org/10.1016/j.ijhydene.2011.01.036.
[112] Milazzo RG, Privitera SMS, Scalese S, Lombardo SA. Effect of morphology and mechanical stability of nanometric platinum layer on nickel foam for hydrogen evolution reaction. Energies 2019;12. https://doi.org/10.3390/en12163116.
[113] Hellmann A, Pitz M, Schmidt K, Haller F, Ripperger S. Characterization of an open-pored nickel foam with respect to aerosol filtration efficiency by means of measurement and simulation. Aerosol Sci Technol 2015;49:16–23. https://doi.org/10.1080/02786826.2014.990555.
[114] Zhang C, Zhou W, Wang Q, Wang H, Tang Y, Hui KS. Comparison of static contact angle of various metal foams and porous copper fiber sintered sheet. Appl Surf Sci 2013;276:377–82. https://doi.org/10.1016/j.apsusc.2013.03.101.
[115] Serov A, Workman MJ, Artyushkova K, Atanassov P, McCool G, McKinney S, et al. Highly stable precious metal-free cathode catalyst for fuel cell application. J Power Sources 2016;327:557–64. https://doi.org/10.1016/j.jpowsour.2016.07.087.
[116] Crosnier S, Rivam R, Bador Vb B. In: Modeling of gas flow through metallic foams, 1st European hydrogen energy conference, september 2–5. France: Grenobel; 2003. p. 1–15.
[117] Tsolas N, Chandra S. Forced convection heat transfer in spray formed copper and nickel foam heat exchanger tubes. J Heat Tran 2012;134:1–10. https://doi.org/10.1115/1.4006015.
[118] Gostick JT, Fowler MW, Pritzker MD, Ioannidis MA, Behra LM. In-plane and through-plane gas permeability of carbon fiber electrode backing layers. J Power Sources 2006;162:228–38. https://doi.org/10.1016/j.jpowsour.2006.06.096.
[119] Martínez-Rodríguez MJ, Cui T, Shimpalee S, Seraphin S, Duong B, Van Zee JW. Effect of microporous layer on MacMullin number of carbon paper gas diffusion layer. J Power Sources 2012;207:91–100. https://doi.org/10.1016/j.jpowsour.2012.01.132.
[120] Yang W, Yang S, Sun W, Sun G, Xin Q. Nanostructured silver catalyzed nickel foam cathode for an aluminum-hydrogen peroxide fuel cell. J Power Sources 2006;160:1420–4. https://doi.org/10.1016/j.jpowsour.2006.02.015.
[121] Langlois S, Coeuret F. Flow-through and flow-by porous electrodes of nickel foam. II. Diffusion-convective mass transfer between the electrolyte and the foam. J Appl Electrochem 1989;19:51–60. https://doi.org/10.1007/BF01039389.
[122] Medraj M, Baril E, Loya V, Lefebvre LP. The effect of microstructure on the permeability of metallic foams. J Mater Sci 2007;42:4372–83. https://doi.org/10.1007/s10853-006-0602-x.
[123] Miwa S, Revankar ST. Hydrodynamic characterization of nickel metal foam, Part 2: effects of pore structure and permeability. Transport Porous Media 2011;89:323–36. https://doi.org/10.1007/s11242-011-9773-2.
[124] Ismail MS, Damjanovic T, Ingham DB, Ma L, Pourkashanian M. Effect of polytetrafluoroethylene-treatment and microporous layer-coating on the in-plane permeability of gas diffusion layers used in proton exchange membrane fuel cells. J Power Sources 2010;195:6619–28. https://doi.org/10.1016/j.jpowsour.2010.04.036.
[125] Holzer L, Pecho O, Schumacher J, Marmet P, Stenzel O, Büchi FN, et al. Microstructure-property relationships in a gas diffusion layer (GDL) for Polymer Electrolyte Fuel Cells, Part I: effect of compression and anisotropy of dry GDL. Electrochim Acta 2017;227:419–34. https://doi.org/10.1016/j.electacta.2017.01.030.
[126] Flückiger R, Freunberger SA, Kramer D, Wokaun A, Scherer GG, Büchi FN. Anisotropic, effective diffusivity of porous gas diffusion layer materials for PEFC. Electrochim Acta 2008;54:551–9. https://doi.org/10.1016/j.electacta.2008.07.034.